

Global Measurements and Hysteresis-Based NPSH Acoustic Approach for the Experimental Study of Cavitation in a Centrifugal Pump

Álvaro Pardo Vigil
José González Pérez
Alberto García Suárez
Jesús M. Fernández Oro
Raúl Barrio Perotti
Mónica Galdo Vega

**Transactions of the ASME,
Journal of Fluids Engineering. ISSN: 0098-2202
November, 2025. Vol. 147, artículo 111205, págs 1-12.**

[DOI: 10.1115/1.4068622]

Global measurements and hysteresis-based NPSH acoustic approach for the experimental study of cavitation in a centrifugal pump

Álvaro Pardo Vigil^(*)

Universidad de Oviedo, Área de Mecánica de Fluidos. pardoalvaro@uniovi.es

Alberto García Suárez^(*)

Universidad de Oviedo, Área de Mecánica de Fluidos. albertogsfp@gmail.com

Jesús M. Fernández Oro^(*)

Universidad de Oviedo, Área de Mecánica de Fluidos. jesusfo@uniovi.es

Raúl Barrio Perotti^(*)

Universidad de Oviedo, Área de Mecánica de Fluidos. barrioraul@uniovi.es

Mónica Galdo Vega^(*)

Universidad de Oviedo, Área de Mecánica de Fluidos. galdomonica@uniovi.es

José González Pérez^(*), ⁽¹⁾

Universidad de Oviedo, Área de Mecánica de Fluidos. aviados@uniovi.es

^(*) Universidad de Oviedo, Área de Mecánica de Fluidos, Campus de Viesques s/n, 33204, Gijón, Asturias, Spain.

⁽¹⁾ Corresponding author. E-mail: aviados@uniovi.es

ABSTRACT

One of the main drawbacks of centrifugal pumps is the reduction of their operation range to avoid cavitation. This undesired phase change phenomenon takes place as a result of high flow velocities attained in the impeller, which locally

reduce the static pressure below the saturation level. Also, certain design features intended to improve pump efficiency in non-cavitating conditions may tend to add even more restrictions to the working range. In the present article, a global measurement of the cavitation characteristics is performed on a test pump, following the traditional performance drop approach, at three different impeller rates of 1800 rpm, 2100 rpm and 2400 rpm. Special stress is made in the discussion of the required Net Positive Suction Head ($NPSH_r$) curves obtained, deviating from common values in centrifugal machines and resembling those of an axial pump at low flow numbers due to the axial inlet with high wrap angle (high angular span of a given blade, from inlet to outlet section) featured by the tested impeller. Afterwards, the study of airborne noise signature is conducted focusing on three working points (namely Q_N , $0.4Q_N$ and $1.7Q_N$, where Q_N stands for the nominal point flow rate) revealing the suitability of both tonal (blade passage frequency) and high-pitch acoustic emission to characterize flow behavior. In addition, cavitation hysteresis is introduced as a novel method to double-check $NPSH_i$ determination. Finally, the acoustically measured $NPSH_i$ and the performance-based $NPSH_r$ are compared to establishing the required safety margin arising from the application of the proposed methodology.

INTRODUCTION

Cavitation is a quite complex phenomenon, with a proper name differing from vaporization and specular to the term boiling, this differentiation being more closely related to the engineering interest on the problem than to a purely thermodynamical criterion. In the literature, cavitation is defined as the formation of vapor bubbles in low pressure regions within a flow, [1]. Alternatively, and following the definition in [2], the term cavitation characterizes the conditions of a point inside a pump where vapor cavities are formed due to a local pressure drop.

A deeper description of the phenomenon is avoided, but the bubble initial stage or nucleation process was established using the Gibbs energy that must be fed to create such bubble in the bulk of the fluid [3], W_b , obtained as:

$$W_b = \frac{16 \pi S^3}{3 (p_v - p_\infty)^2} \quad (1)$$

Where S is the surface tension of the liquid-vapor interface, p_v the vapor pressure and p_∞ the far-field liquid pressure. The nucleation rate, defined as the rate of nucleated bubbles per unit time, is directly proportional to the inverse exponential of W_b following classical nucleation theory [4]. Typically, the critical radius considered for the nucleation events should be of the order of \AA , corresponding to instantaneous intermolecular voids that will later give birth to bigger bubbles.

However, industrial and scientific experience has shown discrepancy with these equations (which would require the liquid pressure to fall below vacuum conditions before bubble formation begins), leading to the development of heterogeneous nucleation theory. Some authors (see [5] for instance) have modelled the nucleation event on a surface instead of in the bulk of a liquid as happening inside a conical cavity that resembles the usual surface roughness imperfections. At the microscopic scale at which the phenomenon is taking place,

surfaces present peaks and valleys whose height and sharpness depend on the roughness profile as depicted in Figure 1.a. This profile is characterized by the crevice angle δ , which is a pure surface characteristic, and the contact angle θ , which depends on fluid-surface coupling.

In these conditions, bubble nucleation will be favored as reaching the same critical radius requires less energy than that estimated from the ideal (spherical one). Even though the equilibrium or critical radius remains the same as for the spherical bubble, the required energy invested for the creation of the bubble in a conical-like surface imperfection (or crevice), W_c , becomes according to [6]:

$$\frac{W_c}{W_b} = \left(\frac{1}{2} + \frac{3}{4} \sin(\delta - \theta) - \frac{1}{4} \sin^3(\delta - \theta) - \frac{1}{4} \cos^3(\delta - \theta) \tan(\delta) \right) \quad (2)$$

Using (2), Figure 1.b is obtained, separating the conditions of bulk and crevice nucleation predominance as a function of crevice sharpness (δ) and liquid-solid contact angle (θ), showing that hydrophobic surfaces ($\theta > 90^\circ$) are more prone to suffer heterogeneous nucleation than hydrophilic ones. There also exists a region of geometries defined by very sharp crevices and highly hydrophobic surfaces in which the bubble nucleation process would be spontaneous if there exists a small enough liquid pressure (bounded by a threshold dashed line in the graph). Luckily, hydrophilic materials are used in most engineering applications and nucleation happens mostly (although not only) in the bulk of the liquid, as crevice nucleation needs the presence of some previous gas pocket in the nucleation site, [7]. When contaminating gases are present in the fluid the whole bubble behavior is altered. In real fluids (i.e., not pure substances), dissolved air concentrations can be significant. This is not especially relevant from the thermodynamic point of view discussed, but is highly influential not only for the nucleation, but also bubble growth processes. If the presence of non-condensable gases is considered, the equilibrium bubble radius R_{eq} is:

$$R_{eq} = \frac{2s}{p_G + p_V - p_\infty} \quad (3)$$

due to the addition of the partial pressure of gas, p_G . This initial gas content allows the existence of microscopic nuclei in the fluid that guarantee the presence of bubbles even at pressures for which the nucleation mechanism is inactive. The dynamics of these bubbles follow the Rayleigh-Plesset equation [7], in which the non-condensable gas is assumed to undergo a polytropic expansion when the pressure of the surrounding liquid p_∞ is reduced:

$$\frac{p_V - p_\infty(t)}{\rho_L} + \frac{p_{G,0}}{\rho_L} \left(\frac{R_0}{R}\right)^{3\gamma} = \frac{3}{2} \left(\frac{dR}{dt}\right)^2 + R \frac{d^2 R}{d t^2} + \frac{4 \mu_L}{\rho_L R} \frac{dR}{dt} + \frac{2 S}{\rho_L R} \quad (4)$$

where R_0 stands for the initial bubble radius, ρ_L is the liquid density and μ_L the liquid viscosity. In this case, and opposite to the case of nucleation in which extraordinary low (negative) pressures need to be attained, bubble growth can happen near the vapour pressure at above-vacuum conditions. The growth and collapse of the bubbles initially present in the working fluid is, therefore, the dominating mechanism governing cavitation. Hence, it becomes straightforward to deduce that water composition, especially in presence dissolved non condensable gases such as air, strongly conditions cavitation performance of pumps and other types of hydraulic machinery. For instance, the studies by [8] proved the major influence of water composition in cavitation phenomena. The distribution of cavitation nuclei, i.e. the bubbles already existing in the fluid at rest in atmospheric conditions, clearly varies with three factors: Fluid temperature, fluid composition and turbulence.

For the application of cavitation studies to centrifugal pumps, the research has been focused on the pump inlet section (impeller eye), where many flow phenomena are mixed and give rise to the bubble formation, [9], [10] or [11], among others. The possibility of flow separation in the spiral casing in the near-tongue region has also been considered [12].

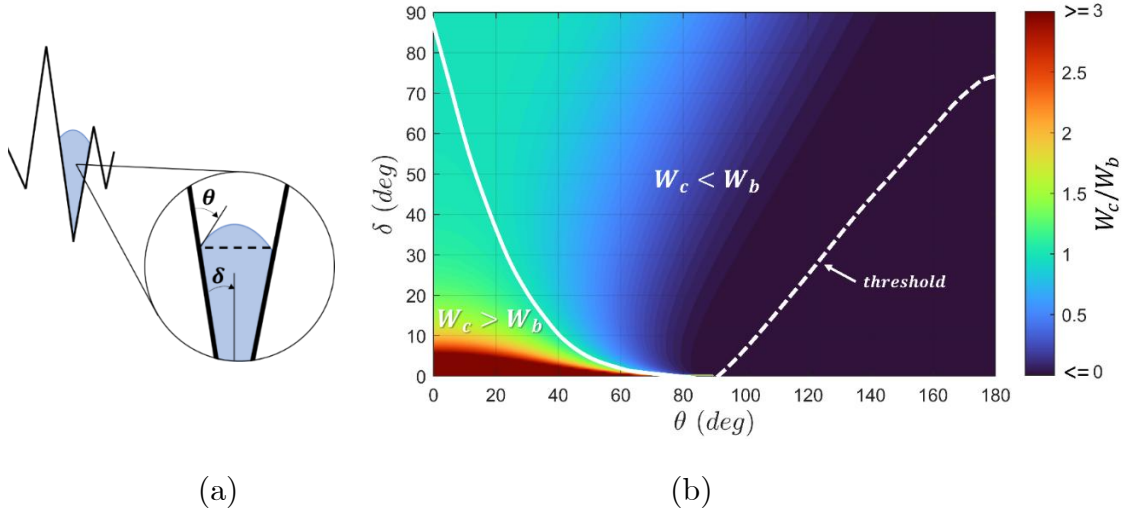


Fig. 1.- Geometry of crevice nucleation in a hydrophilic surface (a) and favorability region of crevice nucleation (b).

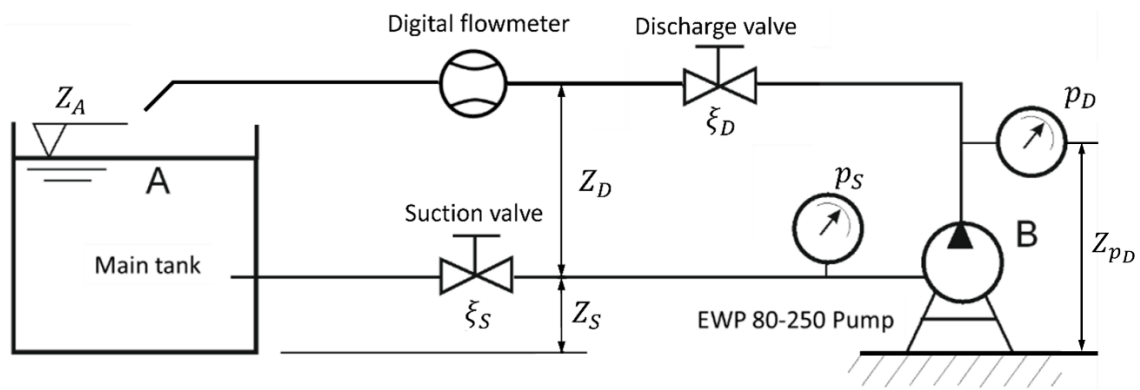
The effects of cavitation, despite being an elusive, non-stationary phenomenon, are usually grouped into a design parameter that allows them to be on the side of safety and thus to avoid their appearance. The *NPSH*, or Net Positive Suction Head, is usually defined for pumps; that is, positive net height in the suction constitutes a measure of the energy (or head, because it is an incompressible flow) available at the suction of the pump above the energy (head or fluid height) that would result in the appearance of cavitation. The definition of the *NPSH* is done with equation (5), which establishes the proximity of the local pressure to the vapor pressure of the liquid. In a practical basis, it leads to:

$$NPSH = \frac{p_1 - p_V}{\rho_L g} + \frac{V_1^2}{2g} \quad (5)$$

where p_1 and V_1 respectively stand for the static pressure and the velocity modulus at the impeller eye, g being the gravity acceleration. At the global average equation (5), the static and dynamic pressure are compared to the vapor pressure to determine the *NPSH* or, in other words, the cavitation margin [13]. Typical parabolic-shape curves are expected for that calculation. In the case of

the available circuit (see Figure 4) and given that the pressure measured by the available manometer is practically at the inlet of the pump, the previous expression (5) is used as stated in the bibliography, [12]. It is intended to obtain the curve of 3% fall, thus indicating a loss of performance of that percentage in the pump head as a result of flow distortions caused by bubble growth, coalescence and nucleation in the form of macroscopic cavities affecting flow patterns. Although a wide variety of criteria can be chosen to determine the *NPSH* corresponding to the start of this performance drop, three main trends can be identified in industrial practice [14], namely 1%, 3% and 5% drops. While the first criterion represents the most conservative option as it characterizes the very beginning of head drop, the last one considers that the *NPSH* required ($NPSH_r$) to avoid cavitation is only felt once a very high decrement of the delivered head has taken place; attending to this reasoning, the 1% criterion would trivially be the best choice but it entails an inherent difficulty related to the impossibility to identify a 1% pressure drop with most pressure gauges installed in pumping facilities. For this reason, the 3% criterion represents a compromise between accuracy and ease of measurement.

$NPSH_r$ curves provided by pump manufacturers attending to the previously defined head drop criteria should be corrected to account for the aforementioned variability factors related to the working fluid temperature and composition. For instance [15] proposed an analytical method to limit undesired vapor volume fractions at the impeller eye using an equivalent $NPSH_r$ which accounted for the dissolved air concentration in the liquid as well as temperature. Additionally, hysteresis represents a new source of variability when dealing with cavitation in turbomachinery flows. As [16] showed in their experiments, with a disk-shaped cavitating headform, once the so-called travelling bubble regime is abandoned in favor of macroscopic supercavitation, hysteretic effects appear and a pressure higher than the one that gave place to the development of such supercavity is needed to recover the original bubbly flow. A distinction is therefore made in the field of turbomachines between the inception and desinence conditions for cavitation [17], the former corresponding to experiments performed at decreasing *NPSH* and the latter at increasing *NPSH*.



(a)



(b)

Fig. 2.- Schematic of the cavitation test rig used for the experiments (a) and real appearance of the facility (b).

Complementarily, a non-dimensional cavitation number σ is proposed in [8] to facilitate comparison between different hydraulic machinery. This parameter only considers the rate between the static pressure terms of the *NPSH* calculation and the inlet dynamic pressure:

$$\sigma = \frac{p_1 - p_V}{\frac{1}{2} \rho_L U_1^2} = \frac{p_1 - p_V}{\frac{1}{2} \rho_L (\omega R_{T,1})^2} \quad (6)$$

where U_1 is the peripheral velocity modulus at the impeller eye, ω the impeller rotation speed and $R_{T,1}$ the impeller eye tip radius. The cavitation number σ at which the effects of cavitation begin to be perceivable at any level is denoted σ_i , or cavitation inception number. Among the different methods that have been proposed to assess cavitation in centrifugal pumps, motivated by the key role it plays on reliability and quietness during operation, the flow visualization has remained a major source of information for inception data, being still employed by modern researchers (see [12] or [17]) to draw information about cavitation inception spots and impeller-volute interactions with the help of stroboscopic lighting or PIV, [18]. Nevertheless, true cavitation inception happens before macroscopic bubbles or cavities are formed and is perceptible in an inchoating state by means of acoustic waterborne high-pitch noise in the suction line, see [19].

Also, the classical experimental methods have gradually been replaced, especially during the earliest design stages of turbomachinery, by CFD modelling. The studies by [20] or the model by [21] were able to predict cavitation inception and development by means of computationally efficient algorithms based on mixture modelling of the multiphase fluid (air, water vapor and liquid water can be included in the simulation), which are nowadays available in most commercial suites. Computational studies of the cavitating flow in turbomachinery still represent an open research field [22], with new implementations being presented and validated [23] by researchers. However, the major influence played on cavitating flows by both the bubble population in the working fluid and the surface finish characteristics represents a challenge to be overcome. Meanwhile, experimental testing of machinery is combined with the initial estimates provided by CFD along the design process.

A bibliographic study shows that there exist five main methods for experimental cavitation assessment:

- Performance drop. For instance, in [24], where appropriate margins, either in terms of *NPSH* ratios or head margins are suggested to be applied by facility designers.
- Efficiency drops, as stated in [25], where it is shown how many pumps experience an efficiency decrease before any perceivable head drop takes place. In other cases, or at different working points, however, the efficiency drop might be delayed with respect to head decrease.
- Fluid borne noise. The FFT spectrum of the pressure signal at certain points of interest, namely the suction line, volute tongue or volute casing, is measured using hydrophones. Hydroacoustic measurements allow accurate identification of cavitation inception, especially from the study of high-pitch and ultrasonic frequencies, see [26].
- Vibration. If accelerometers are used instead of hydrophones, hence the structure-borne noise being measured, high-pitch fluctuations can also be used to monitor cavitation inception, as in [27] or [28].
- Torque/voltage fluctuations. Real-time preventive maintenance systems employing impeller rate variation to tackle cavitation inception are not based on hydrodynamic criteria but on electric signal fluctuations instead. When these signals deviate from their prescribed design values because of changes in the working fluid composition or deterioration of circuit components, an alert is raised by the system indicating the identified fault and its possible causes (not only cavitation, but also blade passage blockage or excessive volumetric losses can be detected), as shown in [29].

The main drawback of airborne sound pressure level data is the increased difficulty of data treatment, as the hydrodynamic effects are not easily separable from the noise produced in electric drives, valves or couplings and bearings; some authors have even implemented neural networks [30] that help to speed up the interpretation of results and the establishment of a characteristic *NPSH*.

The present study is aimed at reducing the difficulty of data analysis by taking advantage of turbulent noise generation mechanisms and the hysteretic

behavior inherent to pump cavitation, while proposing a cost-efficient cavitation inception detection method. In first place, the cavitating behavior of a test pump will be characterized by the industrially widespread performance drop criterion. Subsequently, the study of the airborne noise signature at variable $NPSH$ will be used to find the cavitation inception conditions ($NPSH_i$) that should be avoided during the service life of the machine. Finally, both criteria will be compared in order to establish a safety margin to be compared with the recommendations from ANSI 9.6.1-2012.

EXPERIMENTAL METHODOLOGY

Pump and test rig.

A commercial pump model, namely a Worthington EWP 80-250 pump whose main geometrical parameters are given in Table 1, is analyzed in the present study. The drive system is connected to a frequency variator allowing impeller speeds up to 2400 rpm, this feature being used for the performance-drop characterization of the cavitating flow.

From the specific speed n_s computed using the nominal flow and head coefficients, the machine can be classified as medium head. However, as can be observed in Figure 3, the pump impeller features an axial inlet section with high blade wrap angle in order to diminish shock losses at the impeller eye. The performance characteristics of the machine are represented by means of the non-dimensional head coefficient versus flow coefficient curves presented in Figure 4, in which the variation of the head coefficient ψ is represented in the vertical left axis (black) as a function of the flow coefficient ϕ , ranging from 0 to 0.07 in the horizontal axis. In addition, the total efficiency (in which the volumetric, hydraulic and electric efficiencies of both the electric drive and the frequency variator have been included) is plotted in blue, ranging from 0% to 70 % in the right vertical axis. Both efficiency and head coefficient curves have been fitted to quadratic tendencies following the widespread trend in turbomachinery, [31].

From these, the nominal (best efficiency) point can be found at $\phi_N = 0.039$ and $\psi_N = 0.83$, exhibiting a total efficiency of 60%-64%, depending on the impeller speed.

The experimental facility in which the pump is installed, designed and built according to BS 5316-2, see [32], is schematized in Figure 4.a while its real appearance is shown in Figure 4.b. Water is pumped from the main tank through the suction pipe, fed at a height Z_s of 0.52 m from the bottom while the total liquid level Z_A is above 1.3 m. A butterfly valve located in the suction pipe at 1.5 m upstream with respect to the pump outlet flange promotes a minor loss ξ_s that is used to decrease the *NPSH* in the suction. A vacuum manometer measuring the suction pressure p_s is located at a distance of 0.6 m upstream the impeller eye, while an additional manometer measures the discharge pressure p_D at a height difference of $Z_{pD} - Z_s = 0.5$ m. A discharge valve with variable loss coefficient ξ_D is used to vary the working point of the circuit by increasing the slope of the resistance curve. Downstream from this valve, a KROHNE® IFC 090 digital meter based on magnetic flow measurement is available, see [33]. An orifice plate is also used for double-checking and avoidance of systematic errors, but its measurements will not be considered due to their higher uncertainty when compared to those of the magnetic flowmeter.

Table 1: Centrifugal pump parameters.

Parameter	Symbol	Value
Specific speed	$n_s = \frac{\omega\sqrt{Q}}{(gH)^{3/4}}$	0.39
Impeller type	-	Closed, axial inlet
Impeller inlet tip diameter	$D_{T,1}$	120 mm
Impeller inlet hub diameter	$D_{H,1}$	50 mm
Impeller outlet diameter	D_2	300 mm
Impeller outlet width	b_2	25 mm
Inlet vane tip angle	$\beta_{T,1}$	17°
Inlet vane hub angle	$\beta_{H,1}$	32°
Outlet vane angle	β_2	29°

Number of blades	Z	7
------------------	-----	---

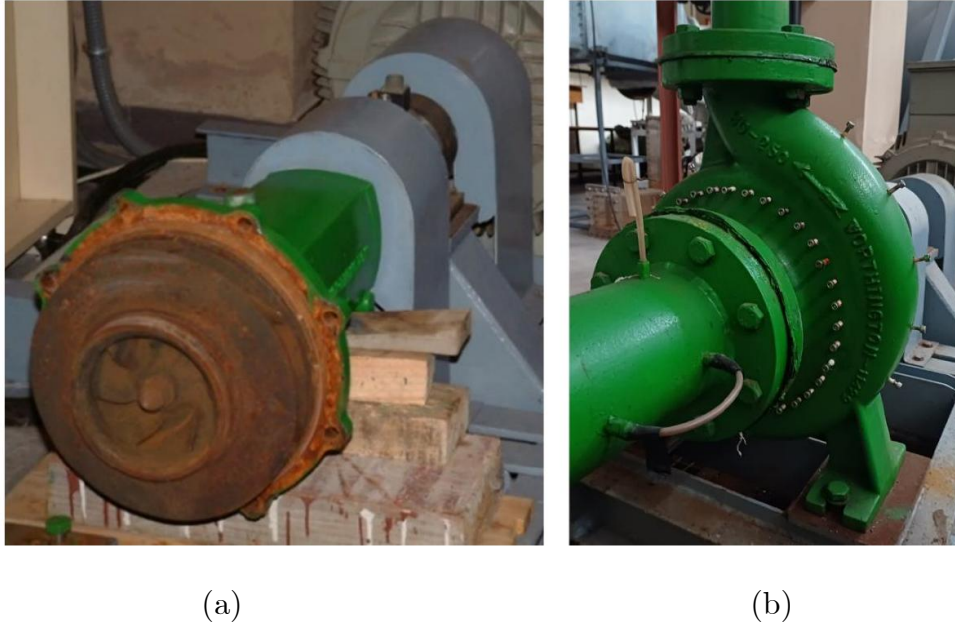


Fig. 3.- Impeller (a) and volute (b) of the test pump.

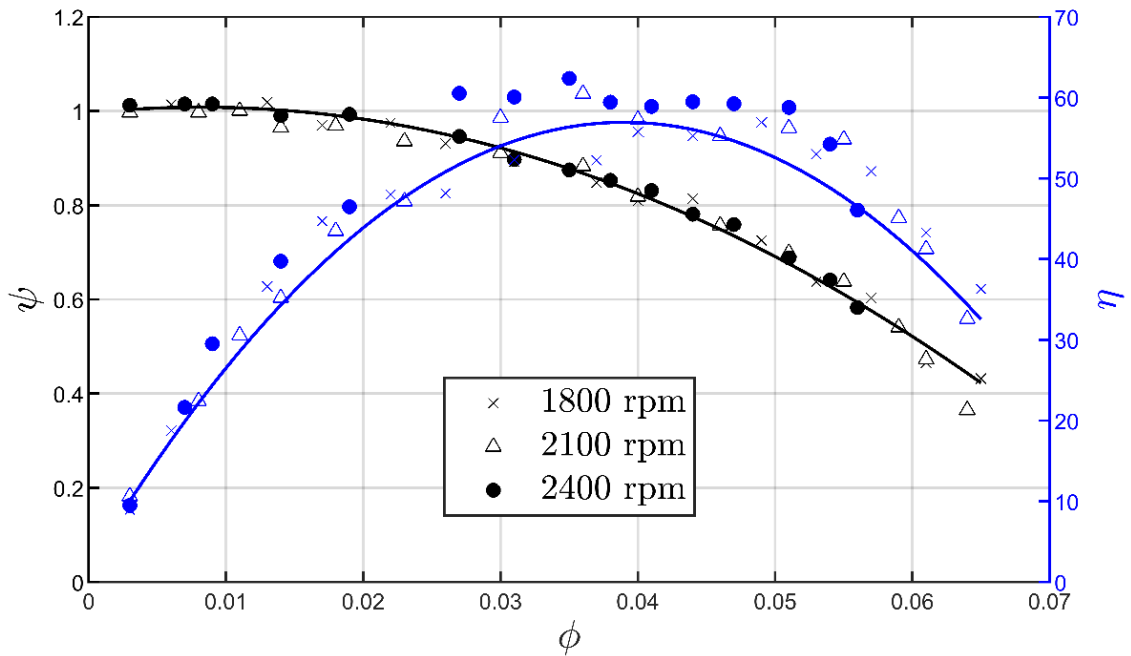


Fig. 4.- Head coefficient ψ (left axis) and efficiency η (right axis) versus flow coefficient ϕ .

The nature and properties of the working fluid are significant factors affecting cavitation measurements, especially due to the strong influence of both water temperature and air content on cavitation inception results; this is the reason why bubble entrainment in suction vortices have been widely studied, see for instance [34]. For this reason, a characterization of the water being pumped has been conducted by means of an indirect method, namely oxygen concentration measurement.

Firstly, the oxygen concentration of a sample taken from the main tank is measured by means of a HACH® HQ meter equipped with a LDO101 probe that is able to measure dissolved oxygen in a sample based on luminescence [35]. The fluid pressure and temperature are also determined in the same measurement, thus allowing to state that the fluid temperature during the performed tests ranged from 15 °C to 17 °C due to water heating as a result of friction in the pumping circuit and fluctuating ambient temperature. In these conditions, the vapor pressure of water ranges from 1.7 kPa (15 °C) to 1.9 kPa (17 °C), see [36], and its value can be established as the average ($p_v = 1.8$ kPa), its uncertainty being found based on a rectangular (uniform) probability distribution according to the Guide for Uncertainty Measurement (GUM) explained in [37], thus resulting in:

$$U_{95}(p_v) = 2 \frac{p_v(16^\circ\text{C}) - p_v(15^\circ\text{C})}{\sqrt{12}} = 0.1 \text{ kPa} \quad (7)$$

The measurement of dissolved oxygen concentration yields a value of 10.22 mg/l at 15.1 °C and 103.6 kPa absolute pressure (sum of atmospheric and hydrostatic terms), thus yielding a mass concentration of 10.23 gO₂/kg water. That can be converted to mass concentration if oxygen solubility in air is known. Although oxygen concentration in air is 21%, this value changes when air is dissolved in water. According to [38], a 36 % solubility of oxygen in air at 15 °C can be considered as long as water is nearly saturated, which is precisely the case

with a 99.4 % oxygen saturation in the sample. Therefore, air content in water is found to be 28.4 ppm. If the air content fraction is defined as:

$$\chi_G = s_{LDO}/[C]_{O_2} \quad (8)$$

Its extended uncertainty, using GUM, would then be (at a 95 % confidence level):

$$U_{95}(\chi_G) = 2 \sqrt{\left| \frac{1}{[C]_{O_2}} \right|^2 u^2(s_{LDO}) + \left| \frac{s_{LDO}}{[C]_{O_2}^2} \right|^2 u^2([C]_{O_2})} \quad (9)$$

For a uniform probability distribution in ± 1 % for the oxygen concentration $[C]_{O_2}$ resulting in a typical uncertainty of $u([C]_{O_2}) = 0.02/\sqrt{12} = 0.006$ and an uncertainty in s_{LDO} of $u(s_{LDO}) = 0.1$ mg/l declared by the manufacturer, the final expanded uncertainty of χ_G yields $U_{95}(\chi_G) = 1.10$ ppm, or a relative uncertainty of 4.8 % which confirms that the sample water is nearly saturated with air, thus favoring the existence of an abundant population of large diameter bubbles.

The airborne sound pressure is measured using a free-field Brüel & Kjær 4189 microphone with 0.2 dB accuracy calibrated at 1 kHz and 94 dB by means of a Brüel & Kjær 4230 pistonphone. Further information about noise measurements is provided in the Acoustic Study section.

The uncertainty of the rest of variables intervening in the experiment is found following the GUM approach for a 95 % confidence level in all cases is shown in Table 2.

Performance study.

A characterization of the cavitating flow behavior in the centrifugal pump is carried out in first place following the widespread industrial approach of head drop, determining the $NPSH$ corresponding to values of 1%, 3% and 5% in $(H_{nc} - H)/H_{nc}$. While 1% head drop $NPSH_r^{1\%}$ is more difficult to spot and thus subjected to higher uncertainty, it is able to predict an early stage of cavitation, and therefore can provide values of $NPSH_r$ greater than those obtained with $NPSH_r^{3\%}$ thus representing a more conservative criterion allowing to design safer facilities. On the other hand, a 5% head drop will be caused by a greater development of cavities in the impeller with respect to the 3% case, meaning that this is a less conservative criterion giving rise to values of $NPSH_r^{3\%} < NPSH_r^{5\%}$. The interest of using different $NPSH$ criteria, however, lies in the comparison of the slopes in the off-design $NPSH_r - Q$ characteristics.

Table 2: Expanded uncertainty (95% confidence level) for the variables of interest in the experiments.

Variable	Instrument	Relative uncertainty (95%)
Flow rate, Q	KROHNE IFC 090 ($\pm 0.3\%$ accuracy)	$\pm 1.5\%$ at Q_N
Pump head, H	Manometers: discharge (0.1 bar scale) suction (0.02 bar scale)	$\pm 1.6\%$ at Q_N
Net Positive Suction Head, $NPSH$	Discharge manometer (0.02 bar scale)	± 0.12 m ($\pm 1.6\%$) at Q_N
Airborne sound pressure, p_a	Brüel & Kjær 4189 free- field microphone (± 0.2 dB accuracy)	$\pm 2.3\%$ (at 0 dB)
Dissolved air in water	HACH LDO101 probe (± 0.2 mg/l)	$\pm 4.8\%$

To obtain the $NPSH_r$ characteristic curves, the inlet pressure in the impeller eye is gradually reduced by closing the suction valve (loss coefficient ξ_s), thus promoting a head loss that reduces the available $NPSH$. At the same time, the flow rate is kept constant by a regulating action on the discharge valve (loss coefficient ξ_d) which allows to restore the working point after it has been altered by an increased slope in the resistant curve of the pumping circuit. This method has been preferred to the regulation of water level in the main tank (used for instance in [26]) due to its higher similitude with industrial pumping facilities. The reduction of $NPSH$ at constant flow rate promotes a gradual loss in the pump head as a result of cavity development, that is then measured for each point until $NPSH_r^{5\%}$ is attained. Even though the water level in the tank remains constant, the maximum available $NPSH_a$ is reduced as flow rate increases due to linear head losses in the pipes. The H - $NPSH$ characteristics are obtained for 9-10 working points ranging from $0.2Q_N$ to $1.7Q_N$ at a given impeller speed, the $NPSH_r$ - Q characteristics arising from their combination. This process is repeated at 1800 rpm, 2100 rpm and 2400 rpm.

Acoustic study.

The cavitating behavior of the test pump has been assessed based on performance drop, which can be measured without the need for specific equipment other than the usual manometers and valves available in any facility. Acoustic analysis, however, is needed to obtain a more meaningful measure of the undergoing flow phenomena and the successive stages of cavitation development. Following the recommendations in [39], a free-field microphone is placed at a distance of 15 cm from the pump volute (tongue side) as shown in Figure 5. This orientation is chosen due to the good results obtained in the past and to the fact that the measurement area is clean from any other noise source, thus reducing the influence of noise coming from other elements in the facility, namely: butterfly valves, discharge to the main tank, electric drive or frequency variators. No machine other than those belonging to the test rig (including the pump-drive assembly and the piping) is working in the laboratory at the same time, the lights

are turned off and only two people conducting the experiment are present in the room (which, in addition, is acoustically insulated thanks to the presence of lead sheets in the doors).

Firstly, ambient noise in the room is measured to establish a baseline to be later quadratically subtracted from the total noise level in order to obtain the acoustic pressure produced by the pump alone, that is:

$$p_a^{Pump} = \sqrt{p_a^{Total} - p_a^{Background}} \quad (10)$$

From these data, the sound pressure level at different suction conditions can also be subtracted from the one at noncavitating conditions so as to isolate the sound caused by cavitation inception alone. It must be noticed, however, that this last technique neglects the influence of cavity growth on the global noise signature, which can alter flow interactions (for instance, between the impeller and the volute) and hence decrease the sound pressure level. This effect is especially noticeable when noise absorption takes place in large cavities below the $NPSH_r^{3\%}$ margin. For this reason, the full noise signature p_a^{Pump} is being used in the present study.

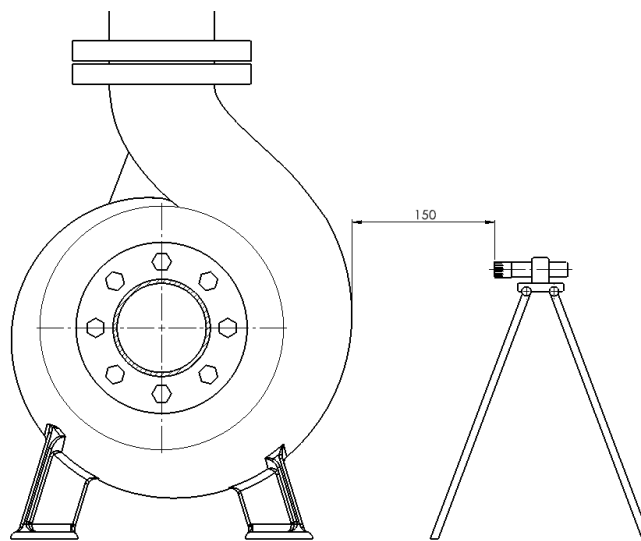


Fig. 5.- Front view of the free-field microphone setup facing the pump volute tongue.

Regarding the signal treatment, data acquisition is performed using a Hanning window, with exponential averaging for the FFT transformation. No filtering has been applied to the signal, as the frequency range of the microphone is already in 6.3-20000 Hz and the studied frequencies range between 350 Hz and 10 kHz. No additional averaging has been performed, and the presented acoustic pressure data are measured for the raw signal after background noise removal.

RESULTS AND DISCUSSION

Performance study.

Although H - $NPSH$ curves for other rotating speeds, namely 1800 rpm and 2400 rpm, were also obtained, only values at 2100 rpm are plotted in Figure 6 for the sake of simplicity (the global trends observed in the latter being also observed in the former). However, the three speed values will be considered hereby in a further analysis. In the dimensional representation from Figure 6.a comparing the delivered head H to the available $NPSH$ at different working points (designated by the ratio between the flow rate and the nominal point flow rate), the head drop is smoothest when the pump works far from its design point, namely at $Q/Q_N = 1.73$ and $Q/Q_N = 0.2$. In these conditions, however, performance drop happens at higher $NPSH$ with respect to the nominal behavior. When operating closest to Q_N , the head drop is sharpest and takes place at lower values of the inlet pressure. In addition, a hump-shaped head increase is spotted before the final performance drop at $Q/Q_N = 1.6$. This phenomenon has already been described in sewage pumps, see [40], but can be extended to thick-bladed (high solidity) and semi-axial (or mixed flow) impellers and inducers. On that kind of geometries, the inlet flow at the impeller eye faces a nearly axial blade arrangement before being directed radially towards the outlet; this is used in heavy duty pumps in order to increase efficiency at the expense of higher manufacturing costs.

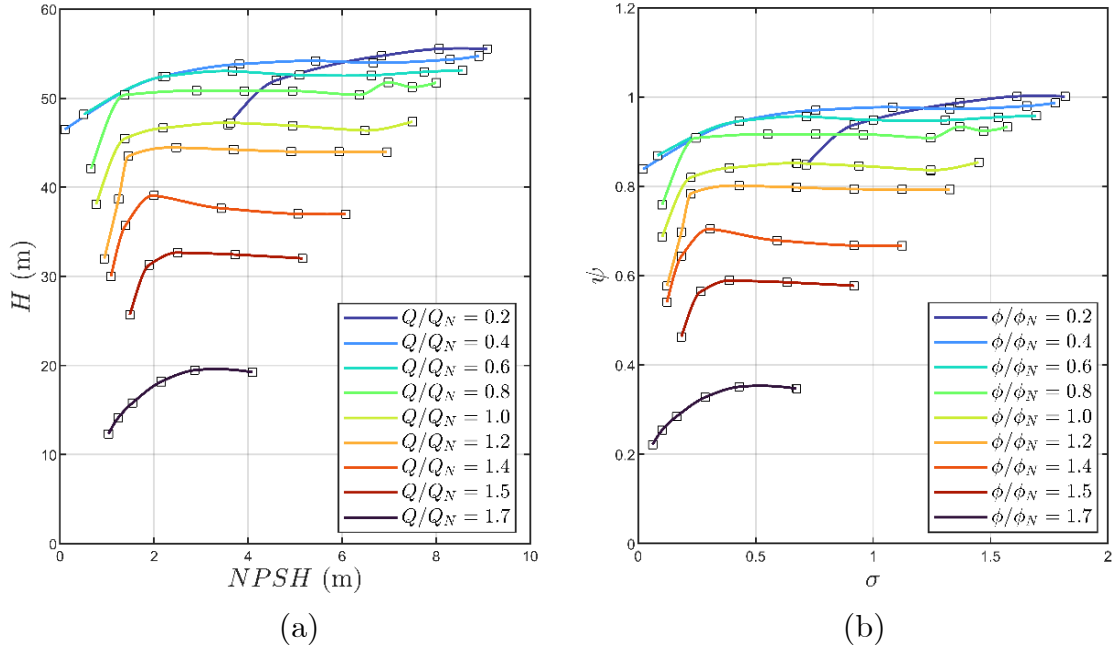


Fig. 6.- Dimensional (a) H - $NPSH$ curves and non-dimensional (b) ψ - σ curves at 2100 rpm.

If the non-dimensional curve showing the variation of the head coefficient ψ with respect to the cavitation number σ (referred to the average impeller eye radial speed for non-dimensionalization) in Figure 6.b is now analyzed, an analogous tendency is observed. Nevertheless, it must be noted that the cavitation number is not merely a non-dimensional form of the $NPSH$ but features a major difference lying on the consideration of only the static (and not the dynamic) pressure terms.

To allow for better interpretation of the results, Figure 7 is built using the data in Figure 6 by gathering the values of $NPSH$ producing a 3% head drop. The behavior at $Q > Q_N$ exhibits the classical tendency of parabolic growth [42]. However, a pronounced increase in $NPSH_r$ takes place at very low flow rates. Such behavior is commonly observed in cavitating analysis of axial pumps [41], where the increase in $NPSH_r$ at flow rates far below the design point differs from the commonly flatter trends that distinguish centrifugal machines. The reason for this difference must be searched in the distinctive high-wrap-angle, near-axial inlet of

this impeller, that makes the low-load cavitating behavior resemble that of axial pumps [1] which suffer partial impeller blockage due to cavity development in the suction side of the blades when secondary flows are promoted by suboptimal attack angles [43]: the $NPSH_r$ characteristics of the EWP 80-250 pump are therefore similar to those of a mixed-flow machine, at least when transferring the air-saturated water (28.4 ppm) containing high populations of large two-phase bubbles that is used as working fluid in the present study.

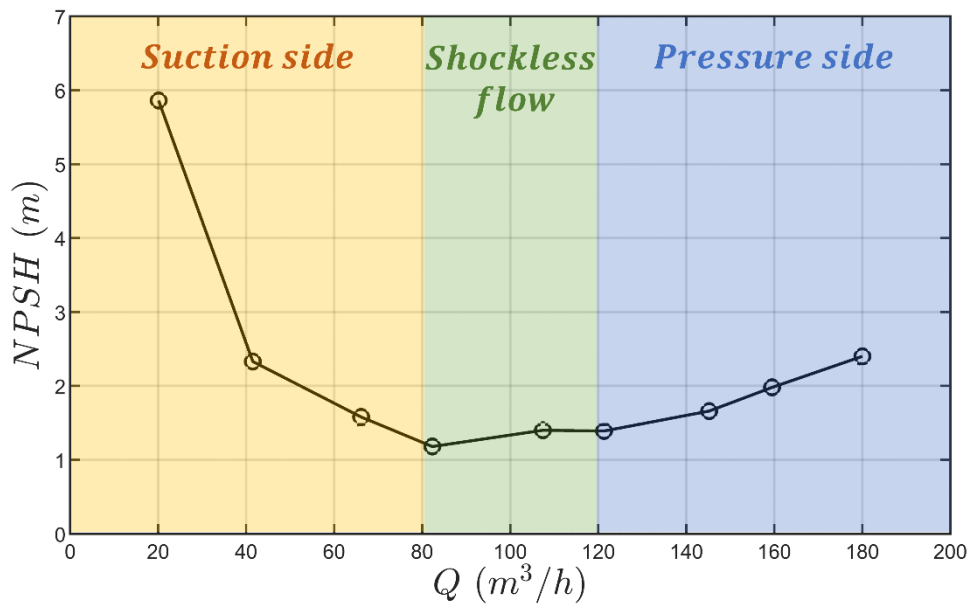


Fig. 7.- Performance-based cavitating characteristics of the centrifugal pump.

Three operating regions can therefore be identified from the cavitating performance point of view, namely:

- a) Shockless flow: When functioning near the design point, flow incidence angle is lowest, and shock losses are reduced. What is more, negligible flow recirculation takes place near the blade leading edge due to the adequate flow guidance characterizing these working conditions. As a result, no vapor pockets appear until the vapor pressure is attained at the impeller eye [44], the head drop being abrupt at this point due to widespread vaporization of the inlet flow.

b) Suction side cavitation: Pure radial centrifugal pumps tend to suffer suction recirculation at the impeller inlet. It is known that as a result of increased flow incidence, cavities appear in the suction side of the blades [45]. Once this happens, streamlines tend to come near at the pressure side of the blades, thus improving inlet angle and reducing shock losses while increasing inlet speed. These factors allow the head drop to be delayed until cavities completely fill the blade passage. In the pump under analysis, however, both the near-axial inlet and the high solidity at the impeller eye prevent this recirculation from happening, the flow incidence angle therefore being increased as the working point deviates from ideal guidance. Thus, vapor pockets are prone to grow on the blade suction side near the leading edge, where pressure is lowest due to the leading-edge vortex, see [46].

c) Pressure side cavitation: As happens in the suction side cavitation region, an increase in flow incidence angle when working at off-design conditions promotes the creation of low-pressure pockets in the leading-edge vortex. In this case, vortices are found in the pressure side of the blades, thus deflecting incoming flow towards the suction side of the adjacent blade and decreasing the overall performance. This is commonly the predominant tendency in centrifugal pumps, in which a nearly parabolic dependence $NPSH_r = f(Q^2)$ is followed at $Q > Q_N$ while suction recirculation flattens the $NPSH_r$ curve in the suction side cavitation region. Otherwise, a U-shaped curve would be obtained.

The described tendencies are replicated analogously when the impeller speed is varied. Figure 8 compares the non-dimensional cavitation characteristics at different rates, showing the cavitation number $\sigma_r^{3\%}$ required to produce a 3% drop in the head coefficient ψ at different working points characterized by their flow coefficients ϕ ($\phi_N = 0.039$ corresponds to the design point). Although the already described parabolic tendency is observed for the three speeds being analysed, the curve slope changes significantly with a consistent tendency entailing a slope decrease in the suction cavitation side of the curve (at $Q < Q_N$) when impeller

rates are increased. In the pressure side cavitation region, however, the cavitation number consistently describes flow behavior at any speed.

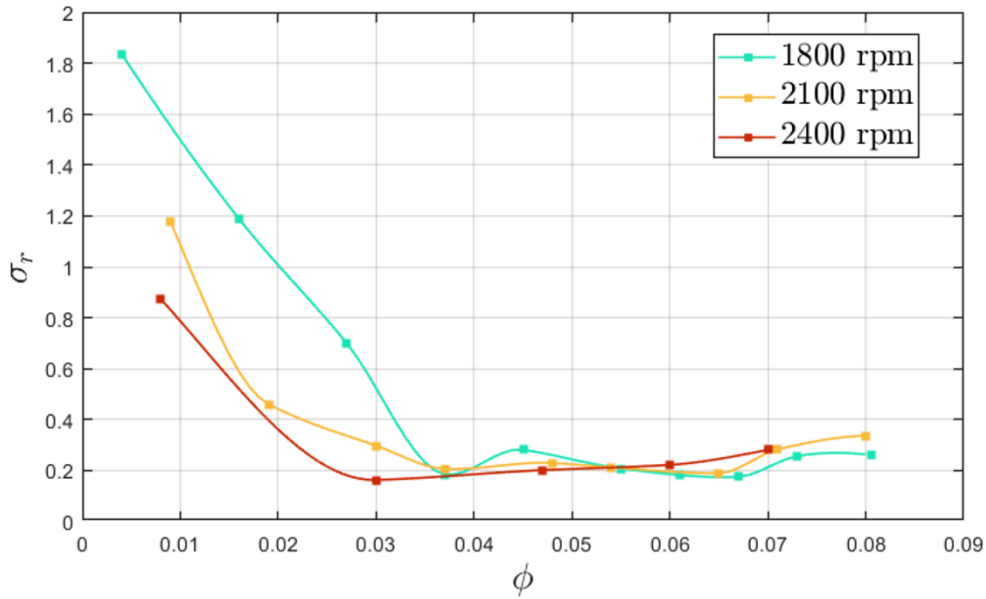


Fig. 8.- Performance-based non-dimensional cavitating characteristics of the test pump at variable impeller speed.

The reason behind the increasing σ_r at low flow rates is the start of head drop at the same inlet pressure for all the rotating speeds being presented. This may be due to a very sharp incidence angle that promotes near-vacuum pressures in the suction side of blades, the *NPSH* required at the impeller eye being the same independently on rotating speed because vacuum pressure represents the lower bound for C_p calculation in these circumstances (the cavitation number is certainly a variation of the C_p assuming that the minimum pressure corresponds to p_v). This is, flow choking is taking place. In these conditions, significant flow recirculation from the impeller outlet to lower pressure regions near the eye can take place, hence leading to the appearance of harmful transient phenomena such as pump surge, see [47]. The evolution of inlet pressure corresponding to 3% head drop is represented in comparison to the dropping σ_r values at the different rotating speeds studied by means of Figure 9, in which the percentage variation of σ_r (choosing the value at 1800 rpm as reference) with increasing impeller rate is plotted for $\phi = 0.08$ and $\phi = 0.03$. While the required cavitation number experiences a 70% decrease, the required inlet pressure remains nearly constant

with just a 10% decrement. It shall be remarked, in addition, that vapor pressure cannot be reduced to a non-dimensional thermodynamic variable and therefore the $p_1 - p_v$ margin defining the cavitation number may remain constant at different impeller speeds, resulting in lower values of σ as U is increased.

Acoustic study.

Figure 10 compares the sound pressure level (in dB) for the three working points being analyzed with the baseline noise level (ambient noise) in the 0-10 kHz range. Background noise levels are negligible above 3 kHz when compared to pump noise, these high-pitch sound pressure levels being the ones preferred for acoustic cavitation inception detection. The *SPL* trend for the different working points coincides with both the classical, shown in [48], and the more recent studies in the field, see [49]. Subtraction of the background noise is considered accurate as long as the difference (in dB) between signals is above 3 dB [50], and the background noise is considered negligible above a 10 dB difference (which represents a halving of the energy).

When the *NPSH* available at the pump inlet is reduced, the noise signature is altered both by the high-frequency noise produced by bubble implosion and by emerging flow interactions caused by cavities. The high-frequency sound pressure level variation with *NPSH* (now in more physically meaningful units of mPa instead of dB) is represented in Figure 11 and Figure 12 by means of a colored contour map in which the frequency spectrum is swept along the horizontal axis at different values of *NPSH* specified in the vertical axis, the highest sound pressure levels being marked in red with blue corresponding to the lowest. While Figure 11 focuses on the evolution of airborne sound pressure level in the range 5-6 kHz at three different working points corresponding to $Q/Q_N = 0.4$ ($Q = 45 \text{ m}^3/\text{h}$), $Q = Q_N$ ($Q = 104 \text{ m}^3/\text{h}$) and $Q/Q_N = 1.7$ ($Q = 180 \text{ m}^3/\text{h}$), Figure 12 shows the spectra corresponding to the 7-8 kHz range.

When comparing the noise signature at the three different working points in the range 5-6 kHz from Figure 11, it can be deduced that there exists a

characteristic cavitation frequency that remains invariable with flow rate and is identified at $f_c = 5250$ Hz. This frequency is not related to macroscopic flow interactions but to fluid properties and should increase when bubble populations are abundant (more implosions would take place per unit time) and bubble radii become smaller (small bubbles have greater resonant frequencies, see [51]). It is therefore consistent with this definition that the sound pressure level is lowest at high $NPSH$ and increases sharply up to a maximum at the highest cavitation damage zone corresponding to bubbly cavitation regime [1], after which bubble implosion rate slows down once blade cavitation begins. In fact, the sound pressure level starts to drop after $NPSH_r^{1\%}$ (white continuous line in the figure) is reached and becomes almost zero after $NPSH_r^{3\%}$ (white dashed line). While sharp sound pressure level evolution with $NPSH$ is observed only at discrete frequencies in the range 5-6 kHz, it must be remarked that this evolution becomes widespread for nearly all frequencies between 7-8 kHz.

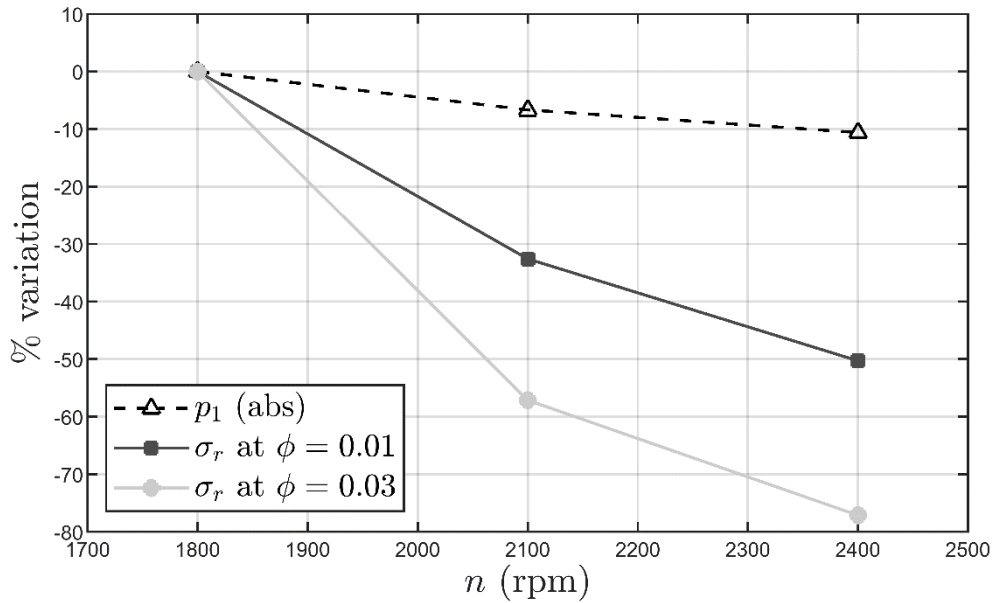


Fig. 9.- Percentage variation of σ_r at low flow rates in comparison to the nearly constant absolute pressure p_1 due to flow choking.

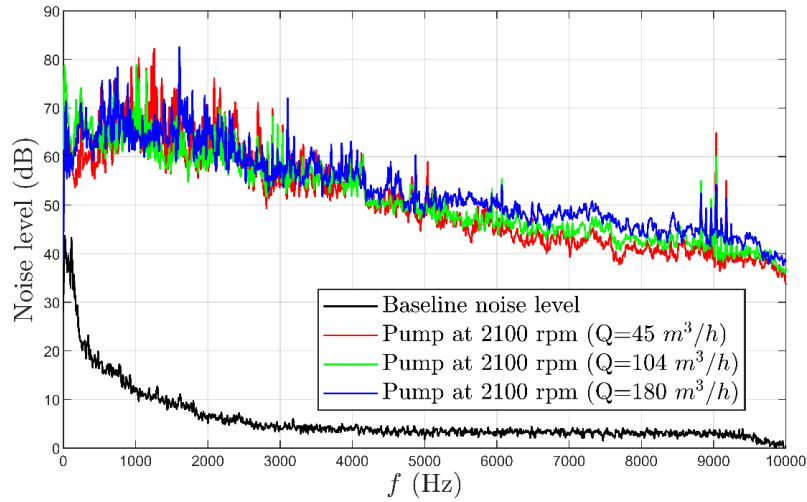


Fig. 10.- Noise level comparison between non-cavitating conditions and baseline noise level with the pump shut off.

It has been shown that the $NPSH$ producing incipient head drop can accurately be deduced from the airborne noise signature. Furthermore, the point of cavitation inception can also be deduced from the joint analysis of Figure 11 and Figure 12. A similar behavior pattern happens at the fluid-characteristic cavitation frequency of 5250 Hz, airborne noise pressure remaining low until a value of $NPSH$ well above the $NPSH_{7\%}$ is attained at the three studied working points. After this, the mentioned sudden increase in noise levels takes place preceding a smoother decline beginning simultaneously with the onset of head drop. An opposite tendency is identified at 5100 Hz, where sound pressure level exhibits a constant value until $NPSH$ falls below $NPSH_i$; at this point, a sudden decrease happens (as can be observed at $Q/Q_N = 0.4$ and Q_N) which is only recovered after head drop is perceivable. As a consequence of the above, the $NPSH_i$ at $Q/Q_N = 0.4$ would correspond to 7.5 m while the $NPSH_i$ at Q_N lies near 5.2 m. Unfortunately, the $NPSH_i$ at $Q/Q_N = 1.7$ cannot be determined as the available test rig does not allow values of available $NPSH$ greater than 4 m at such a high flow rate and only the low- $NPSH$ section the corresponding trends can be spotted in these conditions, meaning that $NPSH_i$ is greater than 4 m for $Q/Q_N = 1.7$.

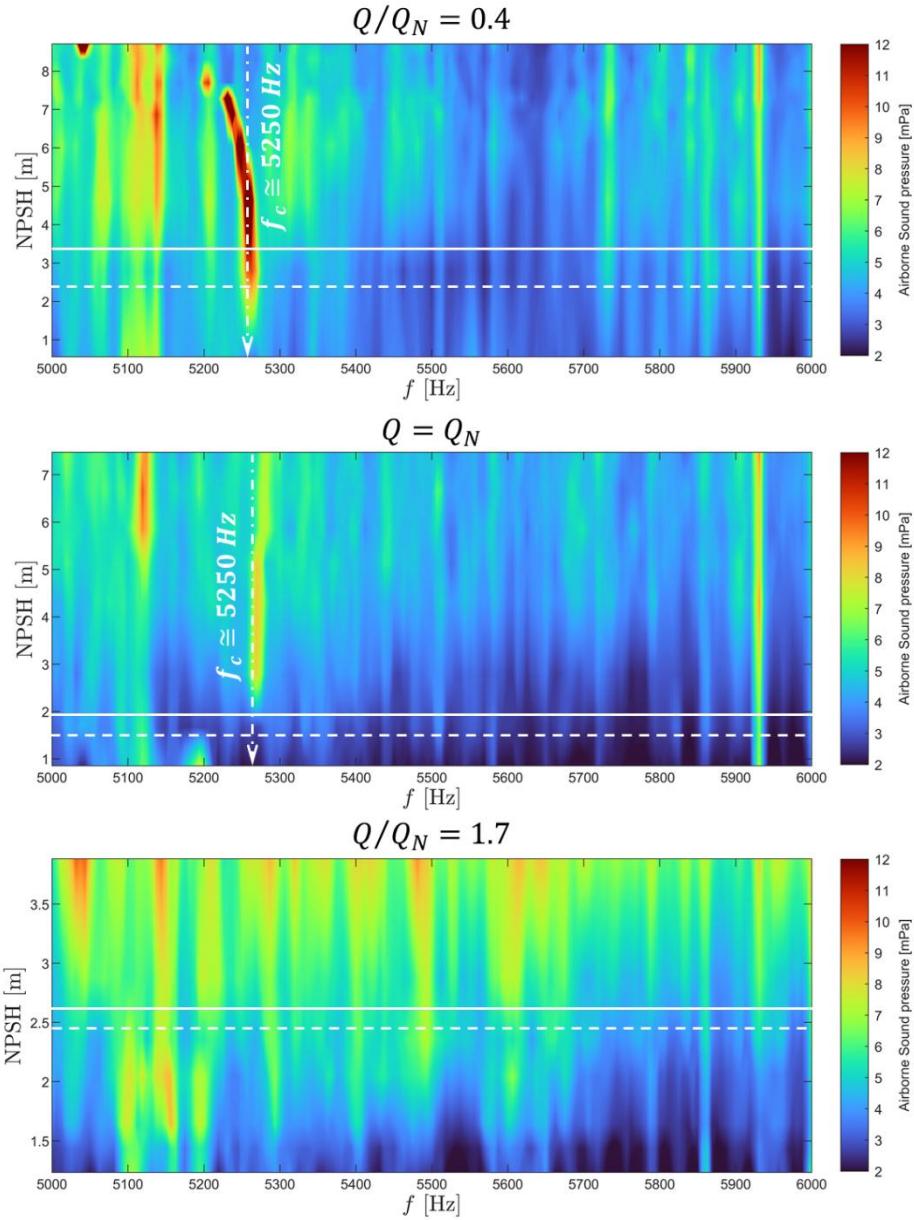


Fig. 11.-Airborne sound pressure variation with $NPSH$ between 5-6 kHz at the three working points analyzed.

Regarding the monotonicity of the airborne SPL evolution, it is smoothest at the nominal working point and sharpest at off-design conditions as a result of leading-edge vortex development. Once cavity nucleation begins in these low-pressure pockets nucleated at the blade tips the flow in their vicinity is immediately disturbed, because of which this variation is registered by the airborne noise signature. When working at the near-optimal conditions of Q_N ,

however, these vortices are smallest and the otherwise sudden flow perturbations are attenuated.

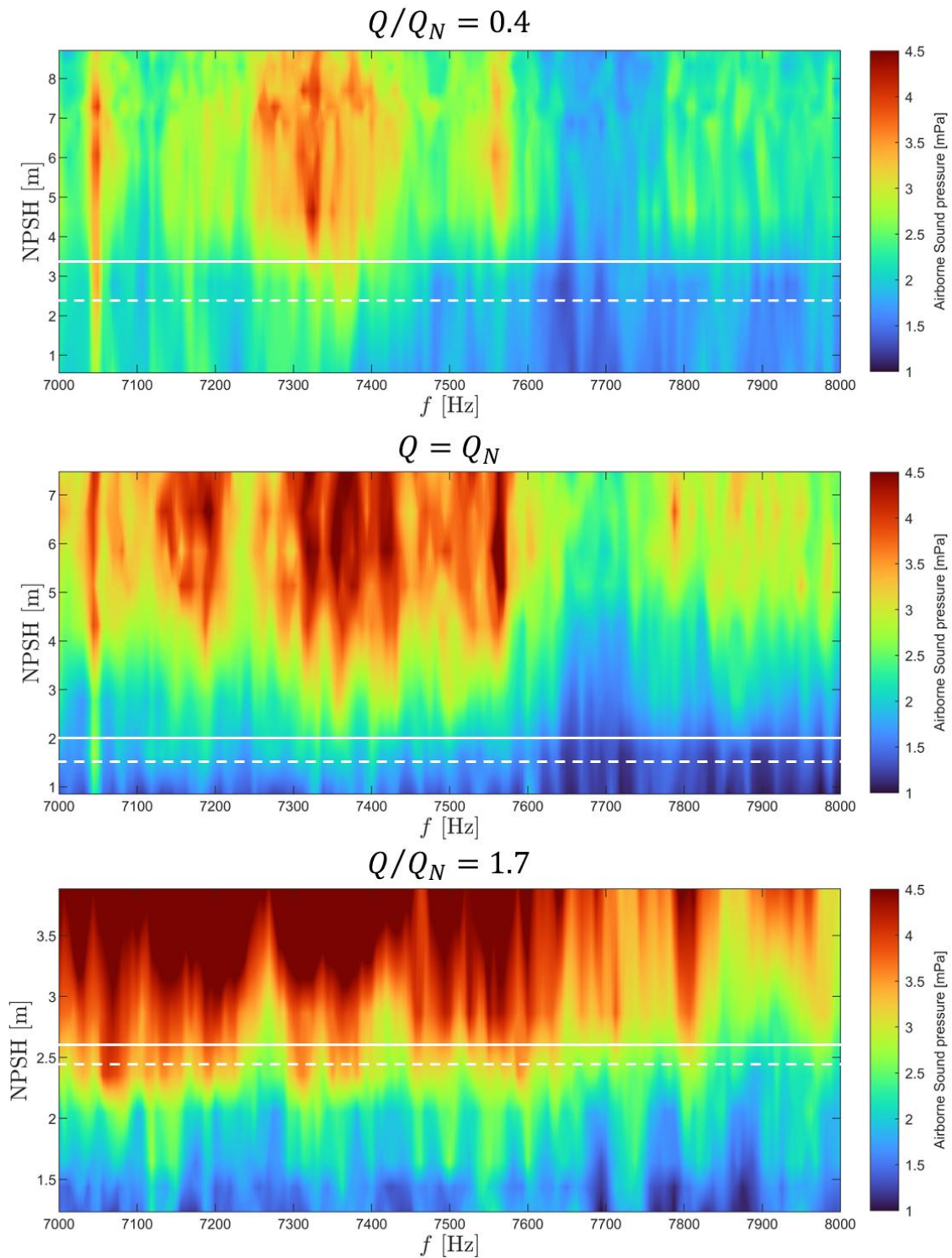


Fig. 12.- Airborne sound pressure variation with $NPSH$ between 7-8 kHz at the three working points analyzed.

It shall also be reminded that, as can be seen in Figure 10, *SPL* differences between the three studied working points become greatest in the range 5-9 kHz, thus reassuring the validity of this frequency range to characterize variations of impeller-rate-independent phenomena in the global noise signature. From the comparison of airborne sound pressure evolution with *NPSH* at different spectral frequencies and working points, it can be stated that head loss is preceded by a decline in the high-pitch noise level. This is not limited, however, to frequencies greater than 5 kHz: it also takes place at the blade passing frequency (BPF) corresponding to 245 Hz when the 7-blade impeller rotates at 2100 rpm, as a result of rotating cavitation. This can be observed in Figure 13, in which the airborne sound pressure evolution at two different frequencies (namely the BPF and 5.25 kHz) is studied both at increasing and decreasing *NPSH* in order to take advantage of the hysteretic nature of cavitation. Continuous lines represent experimental data obtained at decreasing *NPSH*, while dashed lines identify increasing *NPSH*. Due to the oscillation of the fluid-dependent characteristic cavitation frequency with suction conditions, the figure shows an RMS-averaged value of the *SPL* centered in the frequency of interest and sweeping a 10 Hz range instead of the amplitude at the exact Fourier frequency.

Regarding the BPF, smoother *SPL* evolution is observed with decreasing *NPSH*. At the nominal working point, the acoustic airborne pressure progressively increases when approaching $NPSH_i$, attaining a peak at the same *NPSH* as the relative maximum observed for $f = 5250$ Hz, namely $NPSH = 3$ m. A sharper increase in p_a is observed at off-design working points: *SPL* evolution at $Q/Q_N = 0.4$ reaches a peak at $NPSH = 4.7$ m after a constant *SPL* tendency for $NPSH > 6$ m. At 6 m *NPSH*, however, the acoustic pressure rise is not as smooth as in the nominal working conditions, but it experiences a sudden rise instead. The *NPSH* at which these peaks are attained can thus be related to maximum erosion of the impeller, manifested in the form of increased airborne noise.

For the high-load working point $Q/Q_N = 1.7$, the peak observed at BPF noise and 1.4 m *NPSH* must not be misinterpreted: it is not equivalent to the 4.7 m peak in $Q/Q_N = 0.4$ in Figure 13 but to the late uprise described by the *SPL*

curve when NPSH approaches zero in the low-load conditions. This sound pressure rise taking place below $NPSH_r^{5\%}$ at $Q/Q_N = 0.4$ and $Q/Q_N = 1.7$ denotes the onset of a new phenomenon, different from the previously identified ones (namely rotating cavitation at the BPF and travelling bubble cavitation at frequencies above 5 kHz) that increases pump noise when $NPSH$ approaches zero. This event can be identified as pump auto-oscillation according to previous research on unsteady cavitation phenomena [47]. Auto-oscillation is a surge phenomenon that takes place when the fluid velocity field is partially reversed, thus producing backflow as a result of unfavorable pressure gradients arising from transient variations in the delivered head: when the slope of the H vs $NPSH$ curve is steeply negative near performance breakdown, any variation of the inlet pressure (small-amplitude oscillations at the blade passing frequency) causes sudden high-amplitude oscillations in the delivered head leading to a highly transient behavior that undermines the structural integrity of the pump and piping introducing high-strain rate cyclic stresses, as in [52]. This same late-rise tendency was also identified in [53].

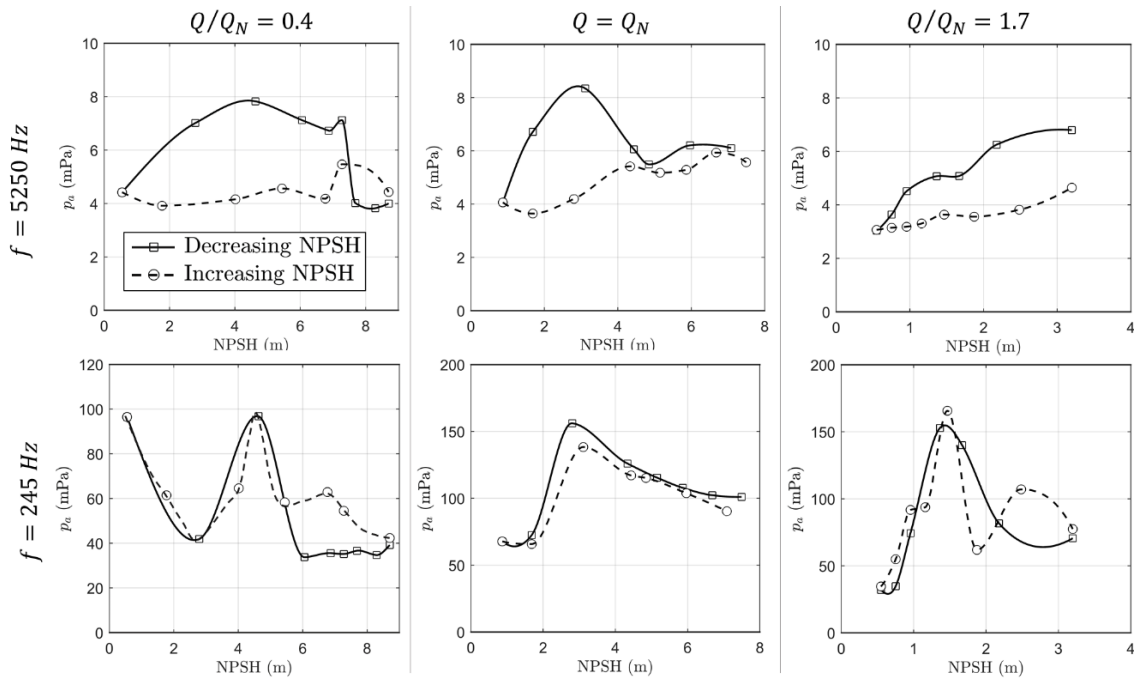


Fig. 13.- SPL evolution with both decreasing and increasing $NPSH$ at $f = 5250$ Hz and $f = BPF = 245$ Hz.

Considering the hysteresis results, a major difference can be distinguished between impeller rate-dependent frequencies and fluid-dependent ones (namely those over 5 kHz): hysteretic behavior is significant at the characteristic cavitation frequency of 5250 Hz, but nearly indiscernible at the BPF. Noise at the BPF is mainly caused by impeller-volute interactions with the jet-wake pattern, whereas high-frequency sound pressure is free from these effects and captures the influence of cavitation bubble noise alone. In spite of this, sound pressure level at the BPF also registers the onset of cavitation at a slightly more developed stage in which cavity development alters such jet-wake pattern and hence changes the impeller-volute interactions at the tongue (and, by definition, shock losses at the impeller eye are also lower in the nominal point). At 5.25 kHz, the *SPL* corresponding to the most developed stage of cavitation being attained (i.e. the lowest NPSH) is maintained when NPSH is raised back until the $NPSH_i$ is overcome. This is true for $Q/Q_N = 0.4$ and $Q = Q_N$; on the other hand, the hysteresis loop is not closed at $Q/Q_N = 1.7$, thus confirming that the available *NPSH* is lower than $NPSH_i$ and showing that cavitation severity is higher at equal values of *NPSH* if the suction pressure has been decreased between both states.

Hence, cavitation hysteresis is found to provide a double-check on cavitation inception. When the NPSH is reduced, the sound pressure experiences two well-defined stages: in first place, acoustic pressure rises as a result of discrete bubble explosions. However, in a more developed stage in which the NPSH is further reduced, the formation of macrocavities decreases the acoustic pressure. Therefore, when the noise signature is being analyzed in an industrial facility with a fixed water level and the NPSH is reduced via the suction valve, only this last (declining) part of the curve may be observed and thus the plant engineer would face the risk of mistaking the absence of cavitation for its most developed stage. However, if the hysteresis approach is applied, then an unclosed hysteresis loop provides additional evidence as observed in the $Q/Q_N = 1.7$ case of the present study.

Up to this point, airborne noise evolution has been analyzed at discrete frequencies in order to draw conclusions about the $NPSH_i$. However, these

distinctive frequencies and especially the fluid-characteristic cavitation frequency may vary when different machines are studied. Although they provide valuable information about flow features, thorough data treatment and analysis is required in order to identify the frequencies of interest. For this reason, a more general and robust measure of airborne noise-spottable cavitation inception is presented as a compendium of the previously discussed criteria. Due to the fact that the *SPL* above 5 kHz is specifically well-suited for cavitation characterization, the whole spectrum between 5-10 kHz is treated as a single waveform with RMS value equal to RMS_{H-P} following Parseval's theorem, see [54], in order to jointly account for all the high-pitch effects of cavitation in the airborne noise signature, that is:

$$RMS_{H-P} = \sqrt{\sum_{f=5\text{ kHz}}^{10\text{ kHz}} (RMS(p_a)_f)^2} \quad (11)$$

The evolution of this equivalent high-frequency RMS amplitude has the shape of a smooth S-shaped curve, as can be seen in Figure 14. Analogously to Figure 13, the sharp drop in *SPL* is preceded by a plateau of constant RMS_{H-P} above $NPSH_i$. In the range 5-10 kHz, airborne sound pressure is lowest at the most developed stages of cavitation and highest prior to inception, from which it can be inferred that fluid-borne noise is being damped by bubble compressibility. From a psychoacoustic point of view, this means that gradual mitigation with decreasing *NPSH* of the high-pitch noise envelope (greatest at cavitation-free conditions) enhances the perception of near-shaft-frequency noise that is more annoying for the hearer. From the observation of the high-pitch *SPL* evolution at $Q/Q_N = 1.7$ it is concluded, once again, that the required *NPSH* exceeds the maximum available one.

Notice as well that by averaging the RMS amplitudes across such a large frequency range, the hysteresis effect is diluted and the RMS_{H-P} trends at increasing and decreasing *NPSH* overlap. At low flow rate ($Q/Q_N = 0.4$), however, hysteretic behavior remains and the increasing *NPSH* curve needs a higher inlet pressure (as happened in Figure 13) to equate the sound pressure measured at

decreasing $NPSH$. This observation coincides with the fact that auto-oscillation hysteresis, as first described by [55], is most prone to happen at low flow coefficients.

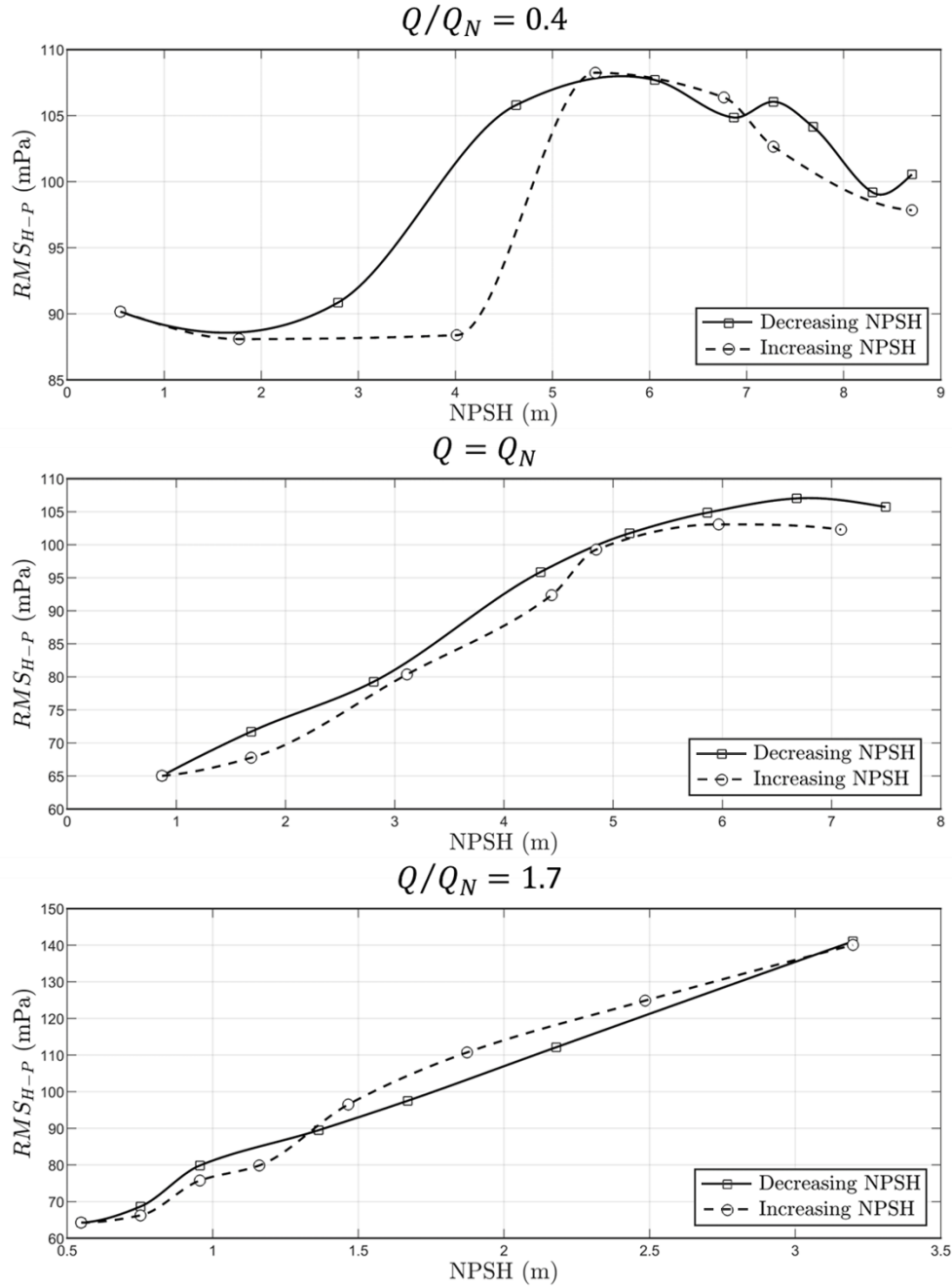


Fig. 14.- RMS-averaged sound pressure levels in the range 5-10 kHz for the three working points analyzed.

The $NPSH_i$ values deduced for the three working points analysed are plotted in Figure 15 together with the $NPSH_r$ obtained under the 1%, 3% and 5% criteria. As expected, the 1% criterion is closest to the $NPSH_i$ curve; however, it

is still advisable to use the $NPSH_r^{3\%}$ due to its lower uncertainty and widespread use. The 5% head drop curve is the flattest, and offers the least information about flow behaviour, although it can be used to specify a safety margin intended to avoid potentially dangerous events such as auto-oscillation. The safety margin of operation, defined as the ratio between the $NPSH$ at which the pump should work in order to avoid the appearance of any cavitation phenomena and the $NPSH_r^{3\%}$, would be equal to 3.22 at $Q/Q_N = 0.4$ and 3.21 at Q_N , both values being significantly over the 1.1 ratio recommended in ANSI 9.6.1-2012 for water transport applications. The global shape of the presented $NPSH_i$ curve is merely illustrative in the pressure side cavitation zone, in which the $NPSH_i$ has been found to lie well above 3.5 m but could not be determined due to test rig limitations; an asymptotic representation is therefore depicted at $Q/Q_N = 1.7$.

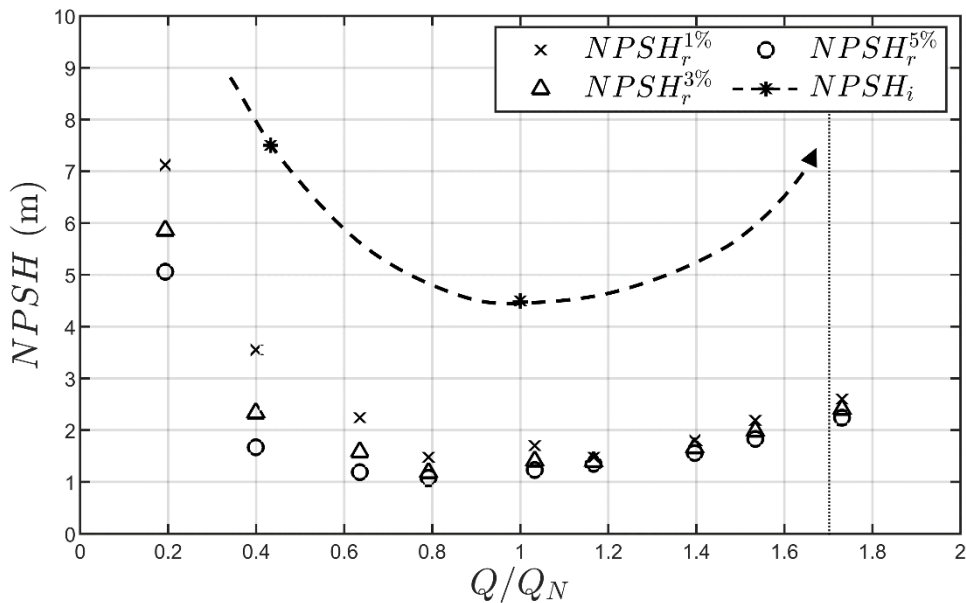


Fig. 15.- Comparison between $NPSH_i$ and $NPSH_r$ at different working points using the 1%, 3% and 5% criteria.

CONCLUSIONS

In this article, a new approach has been adopted towards airborne noise signature assessment of cavitation inception in centrifugal pumps, using sound pressure level evolution with $NPSH$ at different working points. The study is based on a commercial centrifugal pump with an axial inlet and high blade wrap angle. Special attention has been paid to the hysteretic nature of cavitating flows in turbomachinery in order to take advantage of the hysteresis loop closure for a more accurate $NPSH_i$ estimation. Summation of RMS-averaged high-pitch pressure oscillations is also proposed as a robust parameter to characterize the cavitating flow in a centrifugal pump. Data treatment could be automated and sped up by training a neural network with inception and head drop data gathered from different pumps transferring working fluids of variable nature and bubble composition, with the purpose of developing a cavitation assessment app or software.

Non-destructive testing by means of an inexpensive method has been carried out without the need for drilling holes in the pump casing or exposing the integrity both of the pump and microphone. The cavitation characteristics of an axial inlet centrifugal pump have been experimentally determined and discussed, revealing an axial-like behavior in the suction side region of the $NPSH_r$ curves that differs from that observed in most centrifugal impellers: hence, it must be taken into account that the choice of such design feature will influence not only flow guidance and efficiency but also worsen cavitation performance at flow rates below the design point. In addition, transient phenomena such as auto-oscillation may compromise the integrity of either the impeller, the sealing or the coupling resulting from the appearance of unpredicted forces.

The evolution of the dimensionless cavitation performance curves has shown the limited ability of the cavitation number (σ) to characterize theoretically similar working points when the impeller rate is varied. Appearance of near-vacuum areas in the blade passage caused by the leading-edge vortex at extreme flow incidence angles (taking place in the suction side cavitation region, due to the special inlet geometry with high blade wrap angle of the test pump)

represents a lower bound for pressure in non-dimensional basis, the cavitation number hence increasing with decreasing speed while the pressure margin $p - p_v$ remains constant. This is, the flow is choked in these conditions. Nevertheless, the coincidence of the 3% head drop for the cavitation number at the best efficiency point for the three speeds tested shows that its validity still holds if properly interpreted.

Empirical *NPSH* margins intended to avoid cavitation in the design of pumping facilities should also be carefully applied by considering the influence of the working fluid properties (mainly air content and bubble population distribution) and the fluid temperature in the specific application. If safety margins are improperly chosen, there exists a risk of forcing the machine to work in its maximum erosion conditions. Analytic corrections like the one developed in [51] could be applied to the *NPSH_r* curves provided by pump manufacturers to correct the effect of initial air entrainment and pre-existing bubbles.

Some possible pathways for future studies arising from the presented results include CFD simulations of the test pump for broader knowledge of the unsteady impeller-volute interaction producing the airborne noise at BPF, acoustic modelling of fluid-borne cavitation noise and extension of the experimental campaign to different pump sizes and geometries. What is more, a detailed insight into the mechanism of impeller blockage at low flow numbers in axial inlet pumps can be useful in order to provide optimum design guidelines regarding cavitation and pump startup. In the same vein, a joint computational and experimental study of auto-oscillation would be helpful to widen the operation range and increase the service life of hydraulic machinery subjected to intermittent operation. Finally, a study on the influence of bubble population distribution on cavitating behavior would also be useful to establish the bounds of confidence interval for *NPSH_r* safety margins.

Researchers' roles:

Pardo Vigil, Álvaro: Data curation, Investigation, Methodology, Visualization, Writing-Original draft. González, José: Conceptualization, Funding Acquisition, Methodology, Supervision, Writing- Reviewing and Editing. García Suárez, Alberto: Data curation, Software, Validation, Writing-Reviewing and Editing. Fernández Oro, Jesús Manuel: Methodology, Software, Validation, Visualization, Writing-Reviewing and Editing. Barrio Perotti, Raúl: Conceptualization, Data curation, Resources, Software, Writing-Original draft. Galdo Vega, Mónica: Formal analysis, Investigation, Software, Validation.

Acknowledgments:

The first author has obtained a fellowship from the Spanish government (FPU) to carry on with his PhD studies (reference FPU23/03450).

The financial support from the project TED2021-131307B-IOO of the Ministerio de Ciencia e Innovación (Spanish Government) and from the SEK-25-GRU-GIC-23-045 in the frame of the FERES group, from the Sekuens agency (Regional government) are gratefully acknowledged.

The support from the University Institute for Industrial Technology of Asturias (IUTA), through project SV-25-GIJON-1-22, has also helped in the development of the present study.

REFERENCES

- [1] Brennen, C. E., “Hydrodynamics of pumps”. Cambridge University Press; 2011. <https://doi.org/10.1017/CBO9780511976728>.
- [2] Stepanoff, A. J., “Cavitation dans les pompes centrifuges. Pompes centrifuges et pompes helices”, Ed. Dunod, 1961.
- [3] Gibbs, W. A., “The scientific papers of J. Willard Gibbs.” Nature, vol. 75, pp. 361–362, 1907. <https://doi.org/10.1038/075361a0>
- [4] Al Ajmi ,M., Hindmarsh, M., “Thermal suppression of bubble nucleation at first-order phase transitions in the early Universe.” Physical Review D., 106:023505, 2022. <https://doi.org/10.1103/PhysRevD.106.023505>.
- [5] Gallo, M., Magaletti, F., Casciola, C.M., “Heterogeneous bubble nucleation dynamics.” J Fluid Mech., 906:A20, 2021. <https://doi.org/10.1017/jfm.2020.761>.
- [6] Xu, W, Lan, Z, Peng, B, Wen, R, Ma, X., “Heterogeneous nucleation capability of conical microstructures for water droplets”. RSC Adv., vol. 5, pp. 812–818. <https://doi.org/10.1039/C4RA12352B>.
- [7] Brennen, C. E., “Cavitation and bubble dynamics”. Cambridge University Press, 2013. <https://doi.org/10.1017/CBO9781107338760>.
- [8] Lindgren, H., Johnsson, C.A. “Cavitation inception on headforms, ITTC comparative experiments”. 11th International Towing Tank Conference, Tokyo: Akademiförlaget/Gumpert; 1966.
- [9] Schiavello, B., Sen, M., “On the prediction of the reverse flow onset at the centrifugal pump inlet.” ASME 25th Int. Gas Turbine Conference, 261–272, 1980.
- [10] Tan, L., Zhu, B., Cao, S., Wang, Y., Wang, B., “Influence of prewhirl regulation by inlet guide vanes on cavitation performance of a centrifugal pump”. MDPI-Energies, vol. 7, pp. 1050–1065, 2014. <https://doi.org/10.3390/en7021050>.
- [11] Huan, Y., Liu, Y., Li, X., Zhu, Z., Qu, J., Zhe, L., Han., A. “Experimental and numerical investigations of cavitation evolution in a high-speed centrifugal

pump with inducer.” *Journal of Hydrodynamics*, vol. 33, pp. 140–149, 2021.
<https://doi.org/10.1007/s42241-021-0006-z>.

[12] Bachert, R., Stoffel, B., Dular, M., “Unsteady cavitation at the tongue of the volute of a centrifugal pump.” *J Fluids Eng* vol. 132(6), article 061301, pp. 1-6, 2010. <https://doi.org/10.1115/1.4001570>.

[13] Coutier-Delgosha, O., Fortes-Patella, R., Reboud, J.L., Hofmann, M., Stoffel, B. “Experimental and Numerical Studies in a Centrifugal Pump With Two-Dimensional Curved Blades in Cavitating Condition.” *J Fluids Eng* vol. 125, pp. 970–978, 2003. <https://doi.org/10.1115/1.1596238>.

[14] Schiavello, B., Visser F., “Pump cavitation – various $NPSH_R$ criteria, $NPSH$ margins, and impeller life expectancy.” *Twenty-fourth International Pump Users Symposium*, Houston: Turbomachinery Laboratory, Texas A&M University, 2008.

[15] Chen, C., “Cope with dissolved gases in pump calculations.” *Chemical Engineering* 1993.

[16] Ahn, B.K., Jeong, S.W., Kim, J.H., Shao, S., Hong, J., Arndt, R.E.A., “An experimental investigation of artificial supercavitation generated by air injection behind disk-shaped cavitators.” *International Journal of Naval Architecture and Ocean Engineering* vol. 9, pp. 227–237, 2016.
<https://doi.org/10.1016/J.IJNAOE.2016.10.006>.

[17] Perissinotto, R.M., Monte Verde, W., Biazussi, J.L., Bulgarelli, N.A.V., Fonseca, W.D.P., de Castro, M.S., Franklin, E. de M., Bannwart, A.C., “Flow visualization in centrifugal pumps: A review of methods and experimental studies.” *J. Petroleum Sci. and Eng.*, vol. 203, article 108582, 2021.
<https://doi.org/10.1016/J.PETROL.2021.108582>.

[18] Friedrichs, J., Kosyna, G., “Unsteady PIV flow field analysis of a centrifugal pump impeller under rotating cavitation.” *Fifth International Symposium on Cavitation*, Osaka, 2003.

- [19] McNulty, P.J., Pearsall, I. S., “Cavitation inception in pumps.” J Fluids Eng vol. 104, pp. 99–104, 1982. <https://doi.org/10.1115/1.3240865>.
- [20] Singhal, A. K., Athavale, M. M., Li, H., Jiang, Y., “Mathematical basis and validation of the full cavitation model.” J Fluids Eng. Vol. 124, pp. 617–624, 2002. <https://doi.org/10.1115/1.1486223>.
- [21] Schnerr, G. H., GH, M.M., Sauer, J., “Physical and numerical modeling of unsteady cavitation dynamics.” 4th International Conference on Multiphase Flow, New Orleans, 2001.
- [22] Deng, S.S., Li, G.D., Guan, J. F., Chen, X.C., Liu, L. X., “Numerical study of cavitation in centrifugal pump conveying different liquid materials.” Results Phys vol. 12, pp. 1834–1839, 2019. <https://doi.org/10.1016/J.RINP.2019.02.009>.
- [23] Ding, H., Visser, F.C., Jiang, Y., Furmanczyk, M., “Demonstration and validation of a 3D CFD simulation tool predicting pump performance and cavitation for industrial applications.” J Fluids Eng., vol. 133 (1), article 011101, pp. 1-14, 2011. <https://doi.org/10.1115/1.4003196>.
- [24] Schiavello, B., Visser, F. C., “Pump cavitation – various NPSHR criteria, NPSH margins, and impeller life expectancy.” Twenty-fourth International Pump Users Symposium, Houston: Turbomachinery Laboratory, Texas A&M University, 2008.
- [25] Oshima, M., Kawaguchi, K., “Experimental study of axial and mixed flow pumps.” Proceedings of the IAHR Symposium on Cavitation and Hydraulic Machinery, Sendai: Tohoku University, 1963.
- [26] Stephen, C., Arumugam, D., Kumaraswamy, S., “Assessment of noise signature for a cavitating centrifugal pump.” J Energy Resources Technology, vol. 144(4), article 042105, pp. 1-9, 2022. <https://doi.org/10.1115/1.4052618>.
- [27] Lu, Y., Tan, L., Han, Y., Liu, M., “Cavitation-vibration correlation of a mixed flow pump under steady state and fast start-up conditions by experiment.” Ocean Engineering vol. 251, article 111158, pp. 1-9, 2022. <https://doi.org/10.1016/J.OCEANENG.2022.111158>.

- [28] Han, H. S., Jeon, S., Kim, Y., Lee, C., Lee, D., Lee, G., “Monitoring of the cavitation inception speed and sound pressure level of the model propeller using accelerometer attached to the model ship in the cavitation tunnel.” *Ocean Engineering*, vol. 266, article 112906, 2022. <https://doi.org/10.1016/J.OCEANENG.2022.112906>.
- [29] Parrondo, J. L., Velarde, S., Santolaria, C., “Development of a predictive maintenance system for a centrifugal pump.” *J Qual Maint Eng.*, vol. 4, pp. 198–211, 1984. <https://doi.org/10.1108/13552519810223490>.
- [30] Gaisser, L., Kirschner, O., Riedelbauch, S., “Cavitation detection in hydraulic machinery by analyzing acoustic emissions under strong domain shifts using neural networks.” *Physics of Fluids* vol. 35, article 027128, 2023. <https://doi.org/10.1063/5.0137068>.
- [31] McAllister, E.W., “Pipeline rules of thumb handbook”. Gulf Professional Publishing, 2014. <https://doi.org/10.1016/B978-0-12-387693-5.00014-0>.
- [32] British Standards Institution. “BS 5316-2. Acceptance tests for centrifugal mixed flow and axial pumps part 2: Class B tests” 1977.
- [33] Tan, C., Dong, F., “Sensor instrumentation for flow measurement.” *Encyclopedia of Sensors and Biosensors: Volume 1-4, First Edition*, pp. 536–554, 2023. <https://doi.org/10.1016/B978-0-12-822548-6.00074-1>.
- [34] Keller, J., Möller, G., Boes, R.M., “PIV measurements of air-core intake vortices”. *Flow Measurement and Instrumentation* 2014;40:74–81. <https://doi.org/10.1016/J.FLOWMEASINST.2014.08.004>.
- [35] DeGraff, B.A., Demas, J.N.. “Luminescence-based oxygen sensors”. *Reviews in Fluorescence* 2005, Boston, MA: Springer US; n.d., p. 125–51. https://doi.org/10.1007/0-387-23690-2_6.
- [36] Ambrose, D., Lawrenson, I.J., “The vapour pressure of water”. *J Chem Thermodyn* 1972;4:755–61. [https://doi.org/10.1016/0021-9614\(72\)90049-3](https://doi.org/10.1016/0021-9614(72)90049-3).

- [37] Joint Committee for Guides in Metrology (BIPM). “Evaluation of measurement data — Guide to the expression of uncertainty in measurement”. BIPM; 2008.
- [38] Kuiper, G., “Cavitation in ship propulsion”. TU Delft OpenCourseWare; 2012.
- [39] Kercan, V., Schweiger, F., “Cavitation phenomena detection by different methods”. Proceedings of the 6th conference on Fluid Machinery, Budapest: Akademiai Kiado; 1979.
- [40] Thamsen, P.U., Bubelach, T., Pensler, T., Springer P. “Cavitation in single-vane sewage pumps”. International Journal of Rotating Machinery 2008;2008:1–6. <https://doi.org/10.1155/2008/354020>.
- [41] Ng, S.L., Brennen, C., “Experiments on the dynamic behavior of cavitating pumps”. J Fluids Eng 1978;100:166–76. <https://doi.org/10.1115/1.3448625>.
- [42] Al-Obaidi, A.R., “Investigation of effect of pump rotational speed on performance and detection of cavitation within a centrifugal pump using vibration analysis”. Heliyon 2019.<https://doi.org/10.1016/J.HELIYON.2019.E01910>.
- [43] Yun, L., Rongsheng, Z., Dezhong, W., “A cavitation performance prediction method for pumps PART1-Proposal and feasibility”. Nuclear Engineering and Technology 2020;52:2471–8. <https://doi.org/10.1016/J.NET.2020.04.007>.
- [44] Cui, B., Han, X., An, Y., “Numerical simulation of unsteady cavitation flow in a low-specific-speed centrifugal pump with an inducer”. J Mar Sci Eng 2022;10:630. <https://doi.org/10.3390/jmse10050630>.
- [45] Forsthoffer, M.S., “Pumps. Forsthoffer’s More Best Practices for Rotating Equipment”, Butterworth-Heinemann; 2017.
- [46] Kissing, J., Wegt, S., Jakirlic, S., Kriegseis, J., Hussong, J., Tropea, C., “Leading edge vortex formation and detachment on a flat plate undergoing simultaneous pitching and plunging motion: Experimental and computational study”. Int J Heat Fluid Flow 2020;86:108726.

<https://doi.org/10.1016/J.IJHEATFLUIDFLOW.2020.108726>.

[47] Brennen, C.E., “On the dynamics of a cavitating pump”. IOP Conf Ser Earth Environ Sci 2016;49:052018. <https://doi.org/10.1088/1755-1315/49/5/052018>.

[48] Arakeri, V.H., “Contributions to some cavitation problems in turbomachinery”. Sadhana 1999;24:453–83. <https://doi.org/10.1007/BF02745623>.

[49] Mousmoulis, G., Karlsen-Davies, N., Aggidis, G., Anagnostopoulos, I., Papantonis, D., “Experimental analysis of cavitation in a centrifugal pump using acoustic emission, vibration measurements and flow visualization”. European Journal of Mechanics - B/Fluids 2019;75:300–11.

<https://doi.org/10.1016/J.EUROMECHFLU.2018.10.015>.

[50] Staiano, M.A., “Sound level measurements in background noise”. The Journal of the Acoustical Society of America 1991. <https://doi.org/10.1121/1.2029635>.

[51] Shen, Y., Chen, W., Zhang, L., Wu, Y., Kou, S., Zhao, G., “The dynamics of cavitation bubbles in a sealed vessel”. Ultrason Sonochem 2022;82:105865. <https://doi.org/10.1016/J.ULTSONCH.2021.105865>.

[52] Qu, Z., Li, Y., Pan, J., Li, D., Yang, C., Wang, X., et al. “Study on pressure surge characteristics of reactor coolant pump shaft stuck accident condition based on wavelet analysis”. Nuclear Engineering and Design 2022;397:111921. <https://doi.org/10.1016/J.NUCENGDDES.2022.111921>.

[53] Pearsall, I.S., “Acoustic detection of cavitation”. Proceedings of the Institution of Mechanical Engineers, Conference Proceedings 1966;181:1–8. https://doi.org/10.1243/PIME_CONF_1966_181_004_02.

[54] des Chênes, P., “Mémoire sur les séries et sur l’intégration complète d’une équation aux différences partielles linéaire du second ordre, à coefficients constants”. Mémoires Présentés à l’Institut Des Sciences, Lettres et Arts, Par

Divers Savants, et Lus Dans Ses Assemblées Sciences, Mathématiques et Physiques (Savants Étrangers) 1806.

[55] Braisted, D. M., Brennen, C. E., “Auto-oscillation of cavitating inducers.” Polyphase Flow and Transport Technology, 1980.

Nomenclature

Roman letters

$[C]_{O_2}$	Oxygen mass concentration in air dissolved in water (non-dimensional)
f	Frequency (Hz)
f_c	Characteristic frequency (Hz)
g	Standard gravity (m/s ²)
H	Pump head (m) $H = \frac{p_D - p_S}{\rho_L g} + \frac{v_D^2 - v_1^2}{2g} + Z_{pD} - Z_S$
n_S	Pump specific speed (non-dimensional) $n_S = \frac{\omega \sqrt{Q}}{(gH)^{3/4}}$
p	Static pressure (Pa)
p_a	Airborne sound pressure (mPa)
p_1	Impeller eye static pressure (Pa)
p_∞	Local static pressure far from the bubble (Pa)
p_D	Discharge pipe pressure (Pa)
p_G	Compressible gas partial pressure (Pa)
$p_{G,0}$	Compressible gas partial pressure (Pa) when $R = R_0$
p_S	Suction line pressure (Pa)
p_V	Vapour pressure (Pa)
Q	Flow rate (m ³ /s)
Q_N	Nominal point flow rate (m ³ /s)
R	Bubble radius (m)
R_0	Initial bubble radius (m) when $p_G = p_{G,0}$
R_{eq}	Bubble equilibrium radius (m)
RMS_{H-P}	RMS addition of the high-pitch sound pressures (mPa)
S	Surface tension (N/m)
s_{LDO}	Liquid dissolved oxygen solubility in water (mg/l)
t	Time (s)
T	Temperature (°C)
u	Typical uncertainty
U_1	Impeller eye tangential velocity (m/s)
U_{95}	Expanded uncertainty (95% confidence level)
v	Specific volume (kg/m ³)
V_1	Impeller eye inlet velocity (m/s), suction pipe average flow velocity

W_b	Homogeneous bubble nucleation work (W)
W_c	Nucleation work (W) of a bubble in a crevice
Z_D	Discharge line height (m)
Z_{pD}	Discharge pressure gauge height (m)
Z_S	Suction line height (m)

Greek letters

χ_G	Air mass fraction in water (ppm)
δ	Crevice sharpness angle ($^\circ$, deg)
ϕ	Flow coefficient (non-dimensional) $\phi = \frac{Q}{\frac{\pi}{2} b_2 D_2^2 \omega}$
γ	Heat capacity ratio (non-dimensional)
ω	Impeller rate (rad/s)
ψ	Head coefficient (non-dimensional) $\psi = \frac{g H}{\frac{1}{2} \omega^2 R_2^2}$
σ	Cavitation number (non-dimensional) $\sigma = \frac{p_1 - p_V}{\frac{1}{2} \rho_L (\omega R_{T,1})^2}$
σ_i	Inception cavitation number (non-dimensional)
σ_r	Required cavitation number (non-dimensional)
θ	Solid-liquid contact angle ($^\circ$, deg)
μ_L	Dynamic viscosity (Pa·s)
ρ_L	Liquid density (kg/m ³)
ξ_D	Discharge valve loss coefficient (non-dimensional)
ξ_S	Suction valve loss coefficient (non-dimensional)

Acronyms

BPF	Blade Passing Frequency
CFD	Computer Fluid Dynamics
FFT	Fast Fourier Transform
GUM	Guide for Uncertainty Measurement
<i>NPSH</i>	Net Positive Suction Head
<i>NPSH_a</i>	Available NPSH
<i>NPSH_i</i>	Inception NPSH
<i>NPSH_r^{d%}</i>	NPSH required attending to a d% head drop criterion (3% if not specified)
PIV	Particle Image Velocimetry
RP	Rayleigh-Plesset

RMS	Root Mean Square
SPL	Sound Pressure Level